ADVANCED ENERGY MATERIALS
www.advenergymat.de

Mechanistic Understanding of Additive Reductive Degradation and SEI Formation in High-Voltage NMC811||SiO_x-Containing Cells via Operando ATR-FTIR Spectroscopy

*Matthias Weiling, Christian Lechtenfeld, Felix Pfeiffer, Lars Frankenstein, Diddo Diddens, Jian-Fen Wang, Sascha Nowak, and Masoud Baghernejad**

The implementation of silicon (Si)-containing negative electrodes is widely discussed as an approach to increase the specific capacity of lithium-ion batteries. However, challenges caused by severe volume changes and continuous (re-)formation of the solid-electrolyte interphase (SEI) on Si need to be overcome. The volume changes lead to electrolyte consumption and active lithium loss, decaying the cell performance and cycle life. Herein, the additive 2-sulfobenzoic acid anhydride (2-SBA) is utilized as an SEI-forming electrolyte additive for SiO_x-containing anodes. The addition of 2-SBA to a state-of-the-art carbonate-based electrolyte in high-voltage $LiNi_{0.8}Mn_{0.1}Co_{0.1}O_2$, NMC811||artificial graphite +20% SiO_x pouch cells leads to improved electrochemical performance, resulting in a doubled cell cycle life. The origin of the enhanced cell performance is mechanistically investigated by developing an advanced experimental technique based on operando attenuated total reflection Fourier-transform infrared (ATR-FTIR) spectroscopy. The operando ATR-FTIR spectroscopy results elucidate the degradation mechanism via anhydride ring-opening reactions after electrochemical reduction on the anode surface. Additionally, ion chromatography conductivity detection mass spectrometry, scanning electron microscopy, energy dispersive X-ray analysis, and quantum chemistry calculations are employed to further elucidate the working mechanisms of the additive and its degradation products.

1. Introduction

Silicon is one of the most promising next-generation anode active materials, as it offers a nearly ten times higher theoretical gravimetric capacity than graphite, a low delithiation potential, a low voltage hysteresis, as well as relatively low costs.[1] Yet, the widespread commercial application of Si-based anodes is not possible due to the significant difficulties associated with severe volume changes during (de-)lithiation, leading to pulverization and delamination of the active material. Furthermore, the mechanical stress and the exposure of the uncovered anode surface lead to continuous fracture and (re-)formation of the solid-electrolyte interphase (SEI). This accelerates electrolyte degradation and active lithium loss, resulting in a shorter cell cycle life.[2–5]

To minimize the effect of pulverization, graphite blends with understoichiometric silicon oxide (SiO_x, $x < 2$) can be utilized as anode active

M. Weiling, F. Pfeiffer, D. Diddens, J.-F. Wang, M. Baghernejad
Helmholtz-Institute Münster
IEK-12
Forschungszentrum Jülich GmbH
Corrensstrasse 46, 48149 Münster, Germany
E-mail: b.masoud@fz-juelich.de

C. Lechtenfeld, L. Frankenstein, S. Nowak
Meet Battery Research Center Münster
University of Münster
Corrensstrasse 46, 48149 Münster, Germany

The ORCID identification number(s) for the author(s) of this article can be found under https://doi.org/10.1002/aenm.202303568

DOI: 10.1002/aenm.202303568

material.[6] Still, the addition of 20% SiO_x to graphite nearly doubles the specific capacity of the anode. SiO_x benefits from the formation of lithium silicate during lithiation, as its higher-density matrix can reduce the volume expansion to 160% compared to ≈300% of lithiated Si.[6–8] Nevertheless, continuous (re-)formation of the SEI on SiO_x particles in SiO_x-containing electrodes remains a major challenge. Inevitably, these challenges underline the need for improving the SEI properties, i.e., by implementing electrolyte additives.

The knowledge-based development of tailored additives requires a deep mechanistic understanding of the formation process, structure, and composition of the evolving SEI. Moreover, due to the dynamic nature of the SEI on SiO_x-containing anodes, including (re-)formation and dissolution, aging, and conversion, real-time strategies to investigate the interphase under real working conditions are needed.[9–12] To gain a mechanistic understanding of the reactions taking place in the interphase, operando vibrational spectroscopy was employed in some previous studies and also by our group.[9,13–15] Herein, we developed an advanced operando attenuated total reflection Fourier-transform infrared (ATR-FTIR) spectroscopy technique to gain valuable information about the interphase structure and formation mechanism with electrolyte additives on SiO_x. For this, an in-house 3D-printed operando ATR-FTIR spectroelectrochemical cell was designed, based on the internal reflection mode with a silicon wafer as the working electrode, as previously reported elsewhere.[16] In the internal reflection mode, the interphase is characterized from the electrode toward the bulk electrolyte, as the IR beam is passing through the electrode, which allows the suppression of the bulk electrolyte signal. Furthermore, this is combined with an automatic IR incident angle variation accessory, allowing a depth-resolved SEI characterization via a variation of the IR evanescent wave penetration depth. Generally, sulfur-containing compounds are promising SEI additives, as they offer higher oxidation stabilities and lower LUMOs (lowest unoccupied molecular orbitals). Their lower LUMO facilitates their reduction prior to their carbonyl-containing counterparts.[17–19] A large number of sulfur-based additives, like sultones and sulfonates, were already investigated regarding their SEI-forming abilities and the resulting electrochemical cell performances.[18,20] Herein, as a case study combining electrochemical characterization, bulk electrolyte investigation, and interfacial spectroscopy, 2-Sulfobenzoic acid anhydride (2-SBA) is investigated as SEI-forming electrolyte additive toward its electrochemical performance in high-voltage lithium nickel manganese cobalt oxide ($LiNi_{0.8}Mn_{0.1}Co_{0.1}O_2$, NMC811)||artificial graphite (AG)+20% SiO_x pouch cells. Sulfopropionic acid anhydride, which has a similar structure to 2-SBA when excluding the benzene ring, was investigated regarding its SEI-forming abilities by Jankowski et al. and utilized in low-voltage lithium iron phosphate (LFP)||graphite cells. Sulfopropionic acid anhydride demonstrated to enhance Coulombic efficiency (CE) and capacity retention (CR) even more than the state-of-the-art sulfur-based additives ethylene sulfate or propane-1,3-sultone.[17] Furthermore, as shown by Jankowski et al., the introduction of a benzene ring to an additive structure, like ethylene sulfate, further lowers the LUMO and changes the degradation mechanism, when compared to their counterparts without aromatic ring.[19]

As NMC811 is used as cathode material, lithium difluorophosphate (LiDFP) is added as an additional electrolyte additive. LiDFP, which is considered a state-of-the-art additive in electrolyte formulations for high-voltage cell operations, proved to scavenge transition metals (TMs) by complexation in the electrolyte.[21–22] This is necessary to suppress TM electrode crosstalk, which subsequently induces metal plating on TMs deposited sites on the anode surface, leading to micro short circuits and resulting in rapid cell failure also known as "rollover".[22–23]

In this study, it is shown that the cells containing only LiDFP or 2-SBA as electrolyte additive in the baseline electrolyte (BE) exhibit a better electrochemical performance and cycle life compared to the cells containing BE without additives. Interestingly, the cells containing an optimized concentration of both additives exhibit a significantly longer cycle life. This indicates different functionalities and interphase-forming properties of the additives in the cell. Operando ATR-FTIR spectroscopy results show that 2-SBA degrades on the silicon surface via ring-opening of the anhydride group toward different degradation products. These are a combination of sulfonates and sulfinates attached to the benzene ring, which were found to be present with and without carboxylate groups. Additionally, vibrational bands assigned to sulfate were identified, which proves the detachment of the sulfur-containing moiety from the aromatic ring. The electrochemical and operando ATR-FTIR spectroscopy results are complemented with ex-situ ion chromatography conductivity detection mass spectrometry (IC-CD-MS) to investigate the electrolyte-soluble degradation products of 2-SBA. Furthermore, post-mortem scanning electron microscopy (SEM) and post-mortem energy-dispersive X-ray spectroscopy (EDX) are utilized to visualize the topography and analyze the elemental distribution of the electrode surface, respectively. Additionally, density functional theory (DFT) calculations are performed to predict the molecular parameters and putative reaction pathways of 2-SBA degradation, providing deeper insights into the 2-SBA mediated SEI formation mechanisms.

2. Results and Discussion

2.1. Molecular Parameters and Computational and Experimental Electrochemical Stability

The DFT calculated energy for the lowest unoccupied molecular orbital (LUMO) of 2-SBA is -2.48 eV, which is much lower than the LUMO energy of electrolyte solvents ethylene carbonate (EC, −0.09 eV) or ethyl methyl carbonate (EMC, −0.12 eV), as shown in **Figure 1a**. This indicates a favored reduction of 2-SBA, compared to EC or EMC. It has been proven that the presence of an aromatic ring leads to a lowered LUMO and increased highest occupied molecular orbital (HOMO), reducing the HOMO-LUMO gap. Furthermore, the electron density of the reduced product changes from sulfonyl or carbonyl to the aromatic ring, as it is stabilized by delocalization.[19]

The electrochemical stability of 2-SBA in baseline electrolyte (BE, 1 M $LiPF_6$ in EC/EMC (3:7, by weight)) is investigated via cyclic voltammetry. Figure 1b,c show the cyclic voltammograms for BE and BE+2-SBA, respectively, on AG+20% SiO_x electrodes. As can be seen, there are two additional peaks at a potential of 2.05 and 2.50 V versus $Li|Li^+$. Also, the overpotential for AG+20%

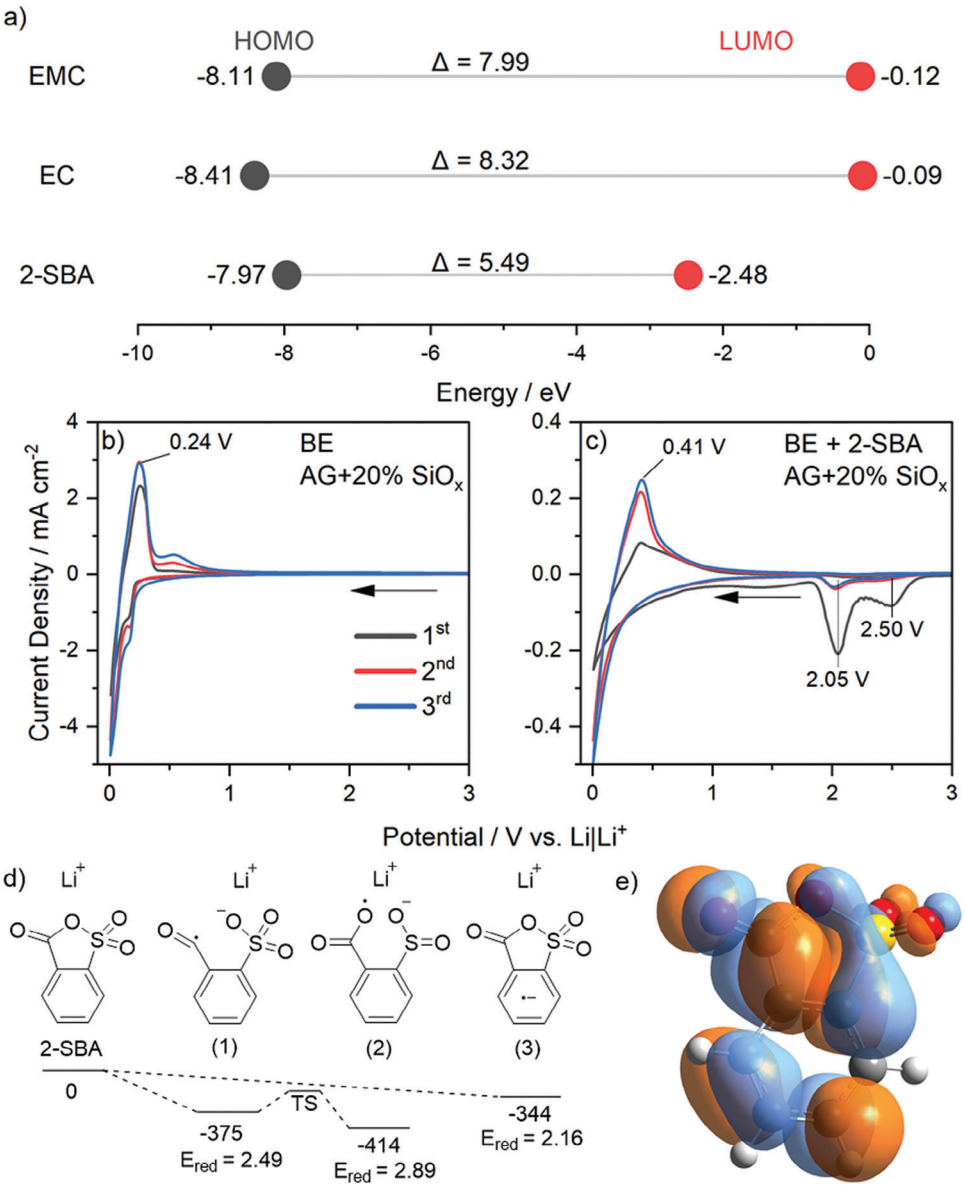

Figure 1. a) Calculated HOMO and LUMO energies in eV of EMC, EC, and 2-SBA. Cyclic voltammograms of cells with AG+20% SiO_x working electrodes with b) BE and c) BE+2-SBA. NMC811 was used as counter electrode and lithium metal as reference electrode. d) Putative reaction path, associated free energy differences ΔG (computed at 298 K) in kJ mol^{-1} and reduction potentials E_{red} in V versus $Li|Li^+$ of the 2-SBA reduction. The energy level of the transition state (TS) from (1) to (2) was not determined. e) illustrated LUMO of 2-SBA.

SiO_x (de-)lithiation is increased for the cells with the 2-SBA containing electrolyte, as the delithiation peak is shifted from 0.24 to 0.41 V versus $Li|Li^+$. This finding indicates the formation of an interphase which raises the overpotential due to increased resistance of the electrode. Moreover, the second and third cyclic voltammetry cycles already show a decreased intensity of the two peaks for 2-SBA degradation, indicating that most of the SEI is formed in the first cycle. Also, there are no new peaks in the following cycles observed, indicating no further oxidative or reductive degradation in high quantity of 2-SBA or its degradation products after initial SEI formation.

The putative reaction path for 2-SBA in Figure 1d is developed by considering similar stages in the reaction paths for sulfopropionic acid anhydride and other sulfur-containing additives with an aromatic ring, as shown elsewhere, suggesting two different reduction paths to a ring-closed and ring-opened structure, whereas the ring is opened first at the C-O bond, followed by a rearrangement to the S-O bond opened structure.[17,19] The calculation of the resulting energy of a putative reduction product of 2-SBA shows ring-opening at the C-O position **(1)**. The corresponding reduction potential for from 2-SBA to **(1)** is calculated to be 2.49 V versus $Li|Li^+$ with an energy gain of 375 kJ mol^{-1}. The S-O opened structure **(2)** would theoretically be formed by 2-SBA reduction at 2.89 V versus $Li|Li^+$, however, the first 2-SBA-related reduction peak in the cyclic voltammogram in Figure 1c begins at around 2.70 V versus $Li|Li^+$ with a maximum at 2.50 V

versus Li|Li$^+$. Thus **(2)** is most likely formed by a rearrangement via a transition state (TS, Figure 1d) of **(1)**. Although the energy gain for reduction to the S-O opened structure **(2)** would be higher than to the C-O opened structure **(1)**, the location of the LUMO might be the determining factor to which bond the additional electron is added. Figure 1e shows, that the LUMO is located at the C-C bond at the carboxyl group, the C-S-O group at the sulfonate, and the aromatic ring, but not at the C-O single bond. The reduction of 2-SBA without ring-opening to structure **(3)** is calculated to occur at 2.16 V versus Li|Li$^+$ with an energy gain of 344 kJ mol^{-1}. This can be assigned to the second reduction peak at 2.05 V versus Li|Li$^+$ in the cyclic voltammogram in Figure 1c.

2.2. Electrochemical Performance Characterization

AG+20% SiO_x cells with NMC811 cathodes filled with baseline electrolyte offer a specific charge capacity of nearly 400 mAh g^{-1} at 1C, which is about twice as much compared to approximately 200 mAh g^{-1} for cells with AG anodes and BE, as shown in **Figure** 2a. This exhibits the potential of incorporating an increased silicon content into the anode active material to increase the energy density of LIBs. However, the cycle life of NMC811||AG+20% SiO_x cells with BE is shorter compared to NMC||AG cells with BE. Thus, failure of the SiO_x-based anode is assumed to be the reason limiting the cycle life in this case. However, the cycle life with just 150 charge/discharge cycles of NMC811||AG cells with BE is relatively short. This is due to the additional constant voltage charging step during charging, which increases electrode active material utilization, but ultimately leads to faster cell failure. For comparison, the same NMC811||AG cells with BE were used in another study by our group, but these were charged without constant voltage step, and showed a lower initial discharge capacity of 180 mAh g^{-1} at 1C, and cell cycle life of ≈500 charge/discharge cycles.[15]

Interestingly, NMC811||AG+20% SiO_x cells with BE and BE+LiDFP show rapidly increasing specific charge capacities (Figure 2a) after cell failure. Instead, cells with BE+2-SBA and BE+LiDFP+2-SBA show decreasing specific charge capacities. It has been proven that a rapid decrease in discharge capacities (Figure 2b) is linked to TM dissolution at the cathode and deposition accompanied by lithium plating on the anode, which then results in increased charge capacities.[24–25] Thus, these cells show rollover failure. However, as shown in Figure 2a, increased charge capacities after cell failure are mostly suppressed for cells containing 2-SBA, which might indicate the suppression of rollover failure in the presence of 2-SBA.

For NMC811||AG+20%SiO_x cells, the specific discharge capacities are shown in Figure 2b. Cells containing the BE and BE+LiDFP show initial discharge capacities of 175 mAh g^{-1} in the first cycle at 1C, whereas the cells with BE containing 2-SBA and LiDFP+2-SBA exhibit slightly lower initial discharge capacities of 172 mAh g^{-1}.

Overall, the cycle life before cell failure, indicated by dropping discharge capacities, or until 80% state-of-health (SoH) is the longest for cells with BE+LiDFP+2-SBA (160 cycles), followed by cells with BE+2-SBA (105 cycles), BE+LiDFP (90 cycles) and just BE (65 cycles). It can be concluded that cells with a dual additive approach of combining LiDFP and 2-SBA prove to have a significantly longer cycle life than cells with each additive separately. Furthermore, the cells with additive-containing electrolytes show a much lower rate of discharge capacity dropping after cell failure, compared to cells without additive-containing electrolyte. This indicates that the additives might play a crucial role in mitigating the ongoing degradation and failure mechanisms in the cells. A comparison with state-of-the-art additives fluoroethylene carbonate (FEC) and vinylene carbonate (VC) is shown in Figure S1 (Supporting Information). In brief, it was observed that cells with BE+FEC exhibit a slightly shorter cycle life than cells with BE with just 56 cycles and slightly higher specific discharge capacities. Furthermore, cells containing BE+LiDFP+FEC exhibit a cycle life of 80 cycles until 80% SoH, but rapidly fading discharge capacities during cycling. The cells with VC show a similar cycle life as cells with 2-SBA.

During galvanostatic charge/discharge cycling, the capacity retentions (Figure 2e) of NMC811||AG+20% SiO_x cells with BE (99.91%), BE+2-SBA (99.92%), and BE+LiDFP+2-SBA (99.92%) are nearly equal. However, cells with BE+LiDFP show lower capacity retention, which decreases after the first 30 cycles from 99.86% down to 99.55% in cycle 90.

The Coulombic inefficiency (CIE) for the first formation cycle and the accumulated Coulombic inefficiencies (ACIEs) for the cells are displayed in Figure 2c,d, indicating the degree of irreversible reactions and active lithium loss in the first formation cycle and during charge/discharge cycling.

The CIE of the first formation cycle is 20.6% for cells with BE and 20.4% for cells with BE+LiDFP, whereas the first cycle CIE for cells containing 2-SBA is 21.9% for BE+2-SBA and 21.3% for BE+LiDFP+2-SBA. Thus, in the presence of 2-SBA, the degree of irreversible reactions in the first charge/discharge cycle is slightly higher. The slightly higher CIE between BE to BE+2-SBA and BE+LiDFP to BE+LiDFP+2-SBA, respectively, may be linked to 2-SBA electrochemical degradation on the anode surface, consuming active lithium in the cell.

Further charge/discharge cycling of cells with 2-SBA-containing electrolytes in Figure 2c also leads to a higher and faster increasing ACIE compared to cells without 2-SBA in the electrolyte. This might indicate a higher quantity of continuous SEI (re-)formation with 2-SBA. Most likely, this occurs on the SiO_x particles, as the volume changes during charge/discharge cycling are more severe compared to graphite.[6] This is in accordance with the SEM images and EDX analysis discussed below, indicating a higher amount of electrolyte degradation products on SiO_x than on AG particles. Overall, cells with BE+2-SBA and BE+LiDFP+2-SBA show more charge consumption compared to cells with BE. The additionally consumed charge indicates more severe parasitic reactions and active lithium loss on the electrode surface, most likely related to SEI (re-)formation.

Usually, 80% SoH is considered end-of-life for first-life applications of commercial cells.[26–27] Nonetheless, NMC811||AG+20% SiO_x pouch cells operating in a voltage range between 4.5 V to 2.8 V with BE already fail at 92% SoH, as shown in Figure 2e. Moreover, only a maximum of 43 Wh g^{-1} accumulated specific energy can be drawn from the cells containing BE until 80% SoH. As already discussed and shown in Figure 2d, cells with BE+LiDFP fade faster than cells with BE, BE+2-SBA, or BE+LiDFP+2-SBA. Nevertheless, 52 Wh g^{-1} accumulated

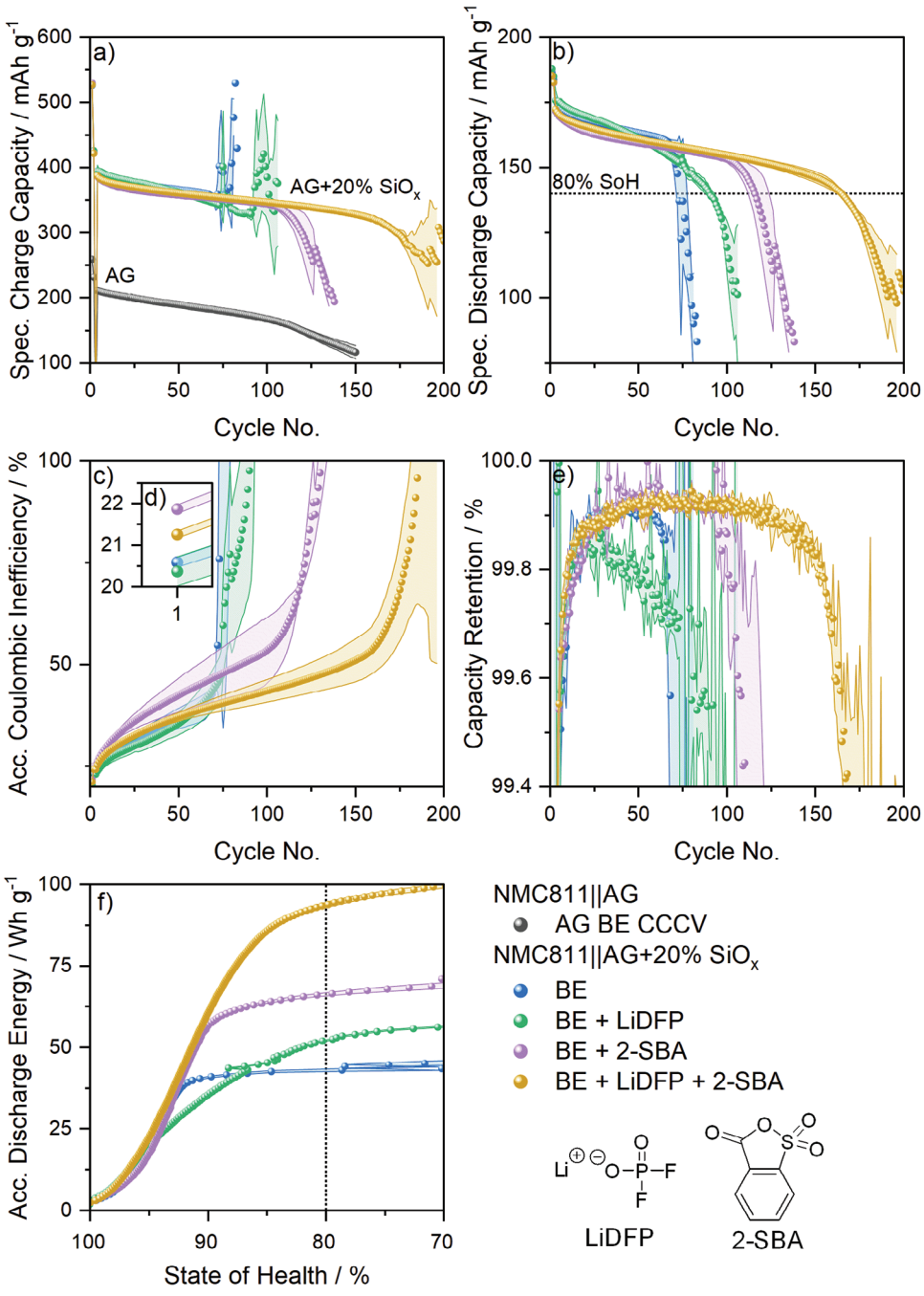

Figure 2. a) Specific charge capacities, b) discharge capacities, c) accumulated Coulombic inefficiencies, d) extracted from c), e) capacity retention versus cycle number, and f) accumulated specific discharge energy density versus state-of-health of NMC811||AG+20% SiO_x cells with BE (1 M $LiPF_6$ in EC/EMC (3:7)) and BE with 0.10 M concentration per additive lithium difluorophosphate (LiDFP) or 2-Sulfobenzoic acid anhydride (2-SBA). Note that the ACIE of cells with BE is similar to cells with BE+LiDFP+2-SBA until cycle 70.

specific energy can be drawn from the BE+LiDFP-containing cells until 80% SoH. With BE+2-SBA and BE+LiDFP+2-SBA accumulated specific energies of 67 Wh g^{-1} and 94 Wh g^{-1} can be drawn from the cells until 80% SoH, respectively.

The internal resistance of the cells caused by interfacial impedance growth and active lithium loss can be indicated by the average charge voltage (ACV) and average discharge voltage (ADV), shown in **Figure 3a**.[13,28–31] Ideally, both should be constant during cell operation and mirror each other.[29] However, as depicted in Figure 3b, the ACV tends to increase while the ADV decreases with the cycle number, leading to higher differential ACV and ADV (ΔV) due to the increased cell resistance. It is clearly shown that in the case of cells with BE, the ACV and ADV change linearly until cell failure, but afterward, the ACV

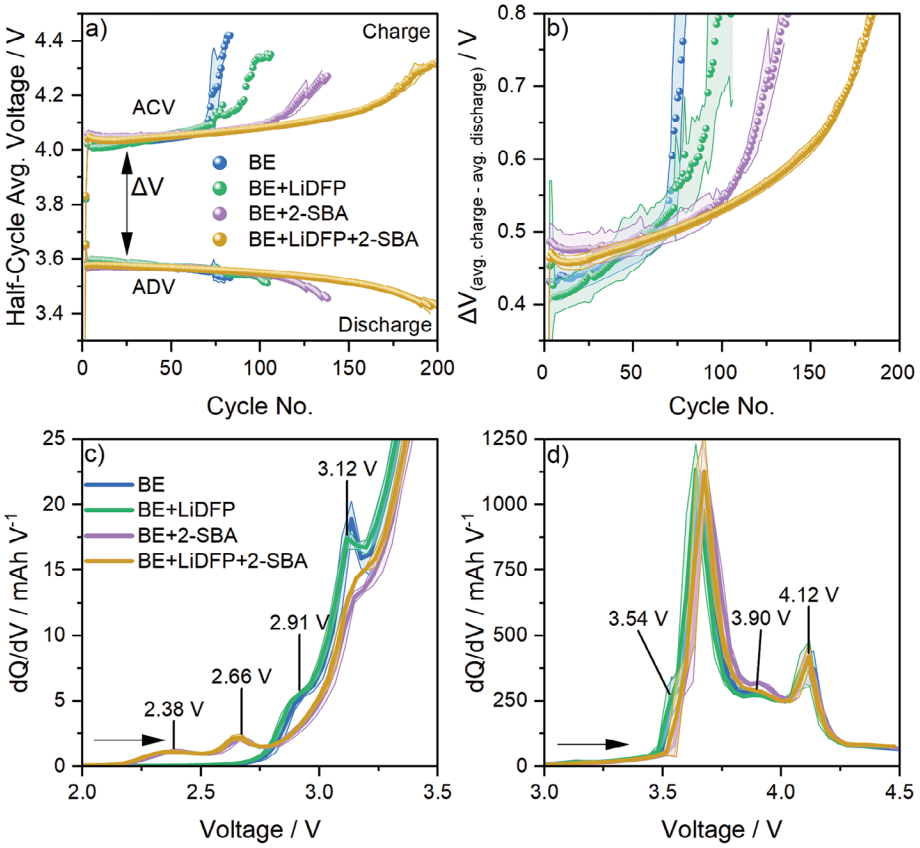

Figure 3. a) Half-cycle average charge and discharge voltage (ACV and ADV) versus cycle number, b) ΔV versus cycle number of NMC811||AG+20% SiO_x cells with BE and LiDFP, 2-SBA, and LiDFP+2-SBA additives. ΔV is calculated by subtracting ADV from ACV. dQ/dV of the charge in the first formation cycle of NMC811||AG+20% SiO_x cells with BE and LiDFP, 2-SBA, and LiDFP+2-SBA additives in a range of c) 2 – 3.5 V and d) 3.0 – 4.5 V.

shows a sharp increase, whereas the ADV changes remain constant. As shown in Figure S2 (Supporting Information), the sharp increase in ACV is due to the increased step time of the constant voltage step during charging and charge capacity associated with anode structural failure and lithium plating.[24] Also, this phenomenon is observed for the cells with LiDFP at slightly higher cycle numbers. According to the studies by Dreyer et al. and Neudeck et al., a stable coating on the cathode by tetraethylorthosilicate and trimethylaluminum will increase the diffusivity and reduce the impedance, leading to improved performance of Ni-rich cathode materials and resulting in improved ADV.[32–33] Thus, it is assumed that the incremental changes of the ACV or ADV are mostly due to processes at the anode or cathode side, respectively.[31–33] Furthermore, the aforementioned ongoing degradation processes during cycling are indicated by incremental changes in ACV and ADV with increasing cycle numbers. Besides, the initial reductive degradation of the electrolyte and SEI formation on the anode is indicated by different initial ACVs.

Compared to cells with BE, cells with LiDFP exhibit a lower initial ΔV due to lower initial ACV and higher initial ADV, but a faster increasing ΔV. This is assumed to be related to improved properties of the initially formed SEI and CEI by the incorporation of LiDFP and the higher amount of lithium-ions in the electrolyte formulation.[22–23,34–35] Albeit, a similar rate of increase in ΔV values between cells containing BE and BE+LiDFP during cycling indicates a similar quantity of degradation processes. In the case of cells with 2-SBA as electrolyte additive, the ΔV is slightly higher in the initial cycles, because of higher ACV. This might indicate a more resistive SEI on the anode formed in the presence of 2-SBA, as observed in cyclic voltammetry investigations in Figure 1c. Furthermore, the ΔV values of the cells increase with a lower rate during charge/discharge cycling in the presence of 2-SBA. Also, the sharp increase in ACV after cell failure is mitigated to a large extent, indicating improved SEI stability and anode active material integrity. This is supported by the absence of a sharp increase in constant voltage (CV) step time at the cycle numbers above 160 for these cells (see Figure S2, Supporting Information).

The influence and activity of LiDFP and 2-SBA as redox shuttle, as reported by Metzger et al., are discussed in the supporting information (Figure S8, Supporting Information).[36–38] The electrochemical performance of cells containing BE and different concentrations of additives are shown in Figures S3–S6 (Supporting Information).

The LiDFP and 2-SBA reactions are electrochemically investigated using differential capacity analysis (dQ/dV), shown in Figure 3c and d. A detailed comparison of dQ/dVs of NMC811||AG+20% SiO_x and NMC811||AG cells with BE is shown in Figure S7 (Supporting Information). As can be seen in Figure 3d during the first charging, cells with BE exhibit multiple

peaks, which can be assigned to AG and SiO_x lithiation, NMC811 hexagonal (H) and monoclinic (M) phase transitions, and electrolyte degradation.[15,39–41] The peak at 3.54 V can be assigned to SiO_x lithiation, which is known to be lithiated before AG.[42] This is also supported by the absence of the peak at 3.54 V in the dQ/dV of NMC811||AG cells (Figure S7a, Supporting Information). Additionally, compared to NMC811||AG cells shown in Figure S7a (Supporting Information), only one broad peak appears in the range of 3.6 to 3.8 V in NMC811||AG+20% SiO_x cells with BE, which can be separated into AG lithiation at ≈3.60 V and NMC811 H1 to M phase transition at ≈3.70 V, respectively. The following peaks at 3.90 V and 4.12 V can be attributed to NMC811 M to H2 and H2 to H3 phase transitions, respectively. Compared to previous studies, the small peaks at 2.91 V and 3.12 V can be linked to the electrolyte solvent reduction.[40–41,43–44] As shown in Figure 3c, there is no additional peak in the dQ/dV of cells containing BE+LiDFP compared to cells containing BE, indicating no additional electrochemical degradation of LiDFP. However, the dQ/dV of the first charge of cells containing 2-SBA in Figure 3c exhibits two additional peaks at a cell voltage of 2.38 V and 2.66 V and less intense peaks at 2.91 V and 3.12 V for electrolyte solvent reduction. It is assumed, that these two peaks correspond to the two peaks which were found in the cyclic voltammograms in Figure 1c. The peak at a cell voltage of 2.38 V in dQ/dV corresponds to the peak at 2.50 V versus $Li|Li^+$ in the cyclic voltammogram. Additionally, the peak at a cell voltage of 2.66 V in the dQ/dV corresponds to the peak at 2.05 V versus $Li|Li^+$ in the cyclic voltammogram. Both peaks can thus be ascribed to the reduction of 2-SBA on the anode following the mechanism given in Figure 1d, which happens before electrolyte solvent reduction.

Besides SEI formation by 2-SBA before EC and EMC, the degree of reductive degradation of EC and EMC species in the first charge is lowered after 2-SBA degradation, which indicates a surface passivation on the anode surface. Additionally, the broad peak between 3.60 V and 3.70 V is shifted to a higher voltage in cells containing 2-SBA, but the peaks at 3.90 V and 4.10 V are not shifted. As already discussed above, the increased anode overvoltage indicates anode or SEI specificity of the 2-SBA additive. Moreover, this shift has a major contribution to the ACV, as shown in Figure 3a.

2.3. Ex-Situ IC-CD-MS Bulk Electrolyte Analysis during Formation

The bulk electrolyte composition of cells containing BE+2-SBA during formation was analyzed by IC-CD-MS to identify the additive degradation products, dissolved in the electrolyte. It should be noted that the detection of compounds in the bulk electrolyte does not necessarily correlate with their presence in the interphase.

Figure 4a–d shows the total ion currents (TICs) as well as the stacked extracted ion currents (EICs) of each identified 2-SBA degradation product at cell cut-off voltages 2.50 V, 2.80 V, 3.25 V, 4.50 V. The proposed 2-SBA degradation product structures are shown in Figure 4e. Complete TICs and an exemplary MS fragmentation are shown in Figure S9 (Supporting Information). The TIC of the BE+2-SBA electrolyte from the cell stopped at 2.50 V in Figure 4a can be divided into three peaks, one by ionic species from the baseline electrolyte at 7.75 min, one by difluorophosphate at 10.14 min, and another by compound **A** with *m/z* 184.9914 at 13.11 min, shown by EIC analysis.[45] Structure **A** results from reductive electrochemical ring opening at the S-O bond of 2-SBA. Here, the hydrogen on the carboxyl group in **A** is most likely related to the chemical environment in the IC column. Furthermore, the methylated and ethylated compounds *m/z* 215.0019 (10.58 min) and 229.0176 (10.72 min) were identified, which can be assigned to compounds **C** and **D**, respectively. Instead of the sulfinate (SO_2^-) headgroup present in compound **A** after electrochemical ring opening, a sulfonate (SO_3^-) head group is observed for each of these two compounds. Compounds **C** and **D** are most likely formed by a nucleophilic attack of an alkoxy group formed from EMC transesterification rather than EMC reductive degradation. Note that the quantitative degradation of EC and EMC occurs at higher voltages, as shown in the dQ/dV in Figure 3c.

All three compounds were also detected in the BE+2-SBA electrolytes at cell cut-off voltages of 2.80 and 3.25 V (Figure 4b,c). While the intensity of compound **A** doubles compared to 2.50 V, due to the increased electrochemical ring-opening reaction, the intensities for compounds **C** and **D** increase by a factor of 10 until 2.80 V and continue to increase up to 3.25 V. This is also evident for both voltages from the emerging shoulder peak arising at higher retention time on the peak corresponding to the difluorophosphate in the TIC at the retention time of 9.87 min. In addition to compounds **C** and **D**, the compounds **E** (*m/z* 303.0180) and **F** (*m/z* 317.0336) are also detected at cell cut-off voltages of 2.80 and 3.25 V, but with substantially lower intensities. The significant increase in intensities of **C** and **D** as well as the emergence of **E** and **F** can be explained by the onset of EMC and EC degradation at 2.80 V in Figure 3c. Therefore, the formation of compounds **C** and **D** might primarily be based on the transesterification of lithium alkoxides derived from the degradation of EMC. Compounds **E** and **F** could be formed by the EC-derived intermediary lithium ethylene monocarbonate (LEMC) as a reactive initiator of a nucleophilic attack.[46–47]

At high voltages (4.50 V, Figure 4d), the formed degradation products prove to be unstable as all signal intensities significantly drop, which becomes especially evident in the TIC. Instead, an intense peak is observed at 8.55 min, which is caused by compound **B** (*m/z* 200.9863), as shown by the EIC. The EIC for *m/z* 200.9863 shows an additional shoulder peak, which can be explained by partial in-source fragmentation of compounds **C** and **D**.

The enhanced formation of compound **B** can be explained by the induced decompositions of compounds **C**, **D**, **E**, and **F**, as well as the oxidative reaction of the ring-opened compound **A** at high voltage. In addition, NMC811 is known to release lattice oxygen at high voltage, due to its high delithiation degree. The released reactive $^1O_2$ oxygen species can then chemically oxidize the 2-SBA.[48–50] Alternatively, the oxidation of the additive can also be catalyzed by a nucleophilic attack of the M-OH hydroxyl groups on the surface of the transition metals.[51–53] Besides NMC, oxygen might also be abstracted from SiO_x particles at the anode.

2.4. Anode Investigation with SEM and EDX

SEM and EDX are employed to visualize the surface structure and elemental distribution of the AG+20% SiO_x anodes

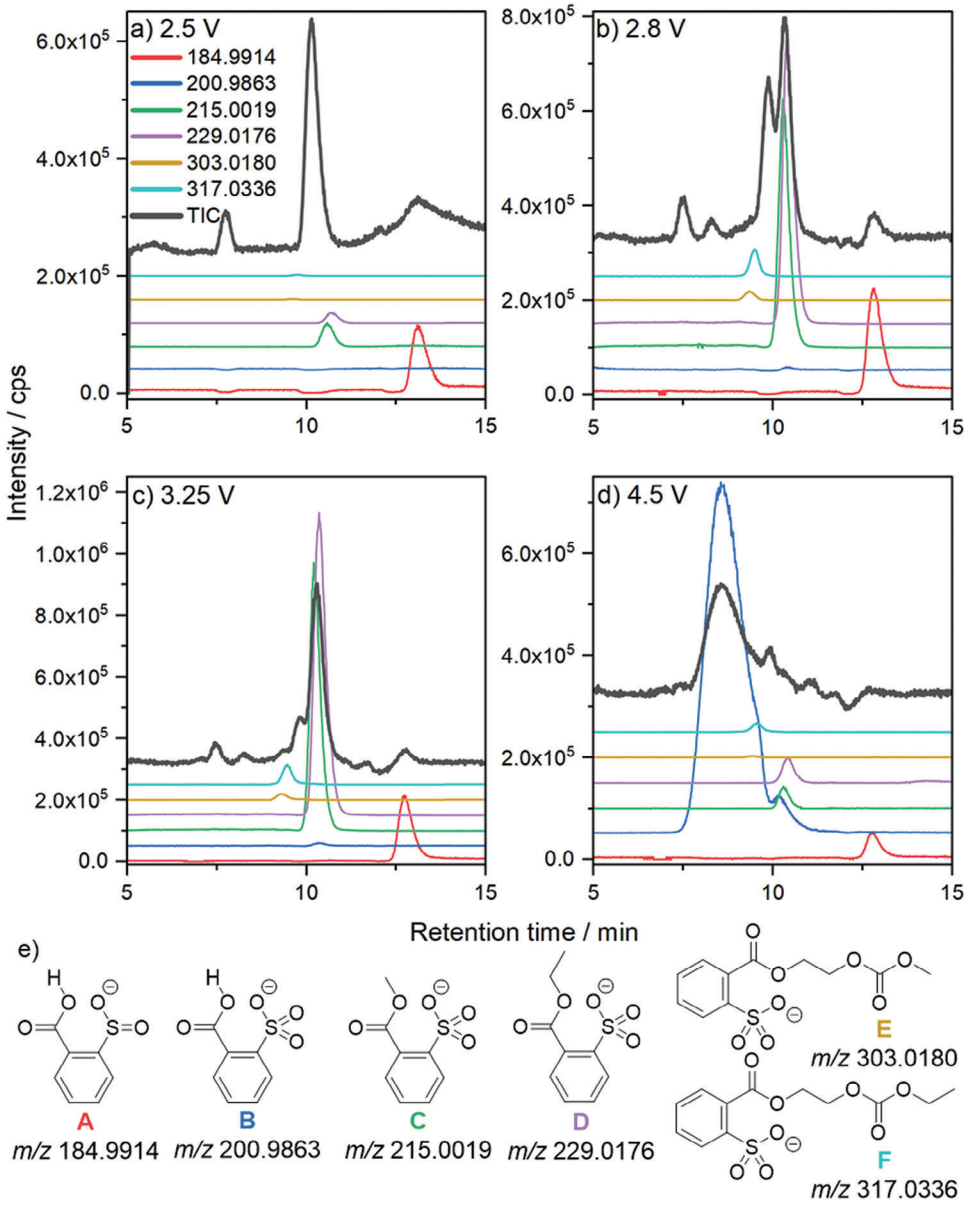

Figure 4. IC-CD-MS chromatogram of the bulk electrolyte extracted from NMC811||AG+20% SiO_x cells with BE+2-SBA after a) 2.50 V, b) 2.80 V, c) 3.25 V, and d) 4.50 V. The TICs were shifted for improved visualization. e) Corresponding structures to the given m/z in a-d.

charge/discharge cycled with BE and BE+2-SBA after cell failure. A comparison of the SEM images in **Figure 5**a,f and the EDX maps of AG+20% SiO_x in Figure 5b,g, respectively, show that the SiO_x particles appear like cauliflower structures with numerous cracks on the surface. Furthermore, Figure 5c,i show the distribution of fluorine on the anode, originating from PF_6 anion and its degradation products. It is indicated that a higher amount of fluorine is present on the SiO_x surface compared to graphite particles due to continuous electrolyte degradation on SiO_x during charge/discharge cycling.

The distribution of sulfur-containing degradation products of 2-SBA in the SEI is evidenced by the EDX analysis of sulfur in Figure 5h. Visual comparison of the SiOx and graphite particles leads to the conclusion that similar to the distribution of fluorine, the amount of sulfur is higher on the SiO_x than on the AG particles. However, the overall intensity of sulfur is lower than that of fluorine, which is most likely due to the ten-fold lower concentration of 2-SBA (0.1 M in the electrolyte) compared to 1.0 M $LiPF_6$ in the electrolyte. Nevertheless, the presence of sulfur proves the presence of 2-SBA degradation products and their incorporation in the SEI.

2.5. Interphase Formation Mechanism Investigation by Operando ATR-FTIR Spectroscopy

The SEI structure and composition are further analyzed by employing a developed advanced operando ATR-FTIR spectroscopy

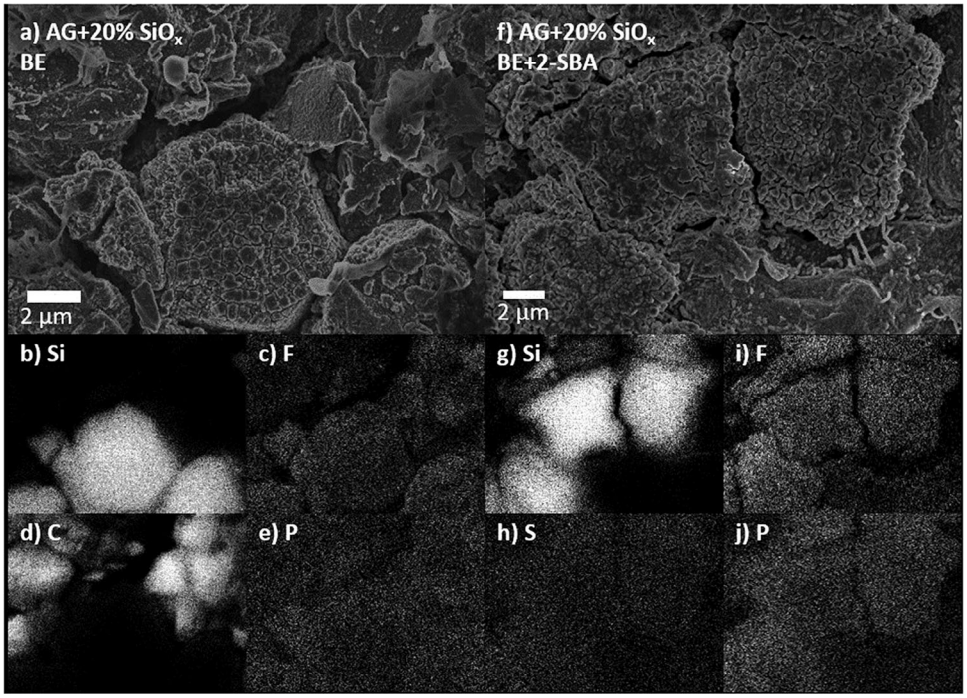

Figure 5. SEM images of the AG+20% SiO_x anodes taken from NMC811||AG+20% SiO_x cells charge/discharge cycled with a) BE+2-SBA and f) BE+2-SBA at a magnification of 5000x. EDX elemental distribution maps showing b) silicon, c) fluorine, d) carbon, and e) phosphorus on image a) BE, and g) silicon, h) sulfur, i) fluorine, and j) phosphorous on image f) BE+2-SBA. The brightness of all EDX elemental distribution maps was increased by 50%.

technique. A detailed description can be found in the experimental section. The composition of the SEI formed by $LiPF_6$ in diethyl carbonate (DEC)/EC on silicon was investigated via in situ ATR-FTIR spectroscopy in previous studies by Shi et al.[16,54] In their study, diethyl 2,5-dioxahexane dicarboxylate (DEDOHC), formed by DEC and EC degradation, was identified as the main electrolyte solvent degradation product component when polarizing the silicon wafer working electrode. The voltage for OHCs formation is located at around 1.5 V. Similar to DEDOHC, other "OHCs", such as ethyl methyl DOHC (EMDOHC) and dimethyl DOHC (DMDOHC), are likely to be formed by transesterification in the presence of EMC.[45,55]

Figure 6 shows the interfacial characteristic vibrational spectra of the baseline electrolyte in contact with the silicon wafer at different IR-wave incident angles during a stepwise sweep of the spectroelectrochemical cell voltage from OCV to 0.005 V including a subsequent 0.005 V constant voltage step for 3 h for lithium insertion. The spectra represent the characteristic regions for OHCs vibrational bands around 1752 and 1262 cm^{-1}, assigned to C = O and C-O stretching (ν) vibrations, and $LiPF_6$ bands at 842 cm^{-1} (ν(P-F)) and 557 cm^{-1} (δ(F-P-F)) at the incident angles between 68° to 35°. With ATR-FTIR, lower incident angles represent a deeper IR penetration depth from the electrode surface toward the bulk electrolyte. As shown in Figure S11 (Supporting Information), by varying the incident angles from 68° to 35° the interphase and the bulk electrolyte can be resolved and monitored separately.

Figure 6a–f show the spectra in the region corresponding to the bands ≈1752 and 1262 cm^{-1} for OHCs. The corresponding peak areas of these bands at selected incident angles are shown in **Figure 7**, indicating the degree of presence of the products at the interphase. The appearance of the 1752 cm^{-1} and 1262 cm^{-1} bands assigned to OHCs at 1.50 V correlates well with the electrochemical response of the spectroelectrochemical cell (Figure S*10, Supporting Information) and with the finding from Shi et al.,[16] confirming the functionality of the spectroelectrochemical cell. The increasing intensity of the bands at high incident angles at 1752 and 1262 cm^{-1} during constant voltage exhibit more OHC formation and accumulation on the SiO_x surface.

By deeper penetration of the formed interphase during 0.005 V constant voltage, the intensities of the peaks corresponding to the bulk baseline electrolyte compound EC increases. Generally, at the surface during voltage sweep and constant voltage hold a higher amount of coordinated than uncoordinated solvents with lithium-ions is observed. The corresponding calculated vibration frequencies for DMDOHC, EMDOHC, and DEDOHC are given in Table Figure S2 (Supporting Information) and the bulk spectra of DMDOHC and DEDOHC are shown in Figure S*12 (Supporting Information) for comparison.

The intensity of the bands at 842 cm^{-1} for ν(P-F) and 557 cm^{-1} for δ(F-P-F), shown in Figure 6g–l, exhibit an overall decreasing trend when lowering the cell voltage. Especially the band for δ(F-P-F) is almost diminished completely, whereas the ν(P-F) band is still visible. This might be due to its intrinsically higher intensity compared to δ(F-P-F), or it may be caused by the accumulation of PF_6 degradation products like organofluorophosphates or lithium fluoride at the interphase, depleting the interphase layer from PF_6 anions.

According to previous studies, a plausible reaction mechanism is the ring-opening of the anhydride after electrochemical

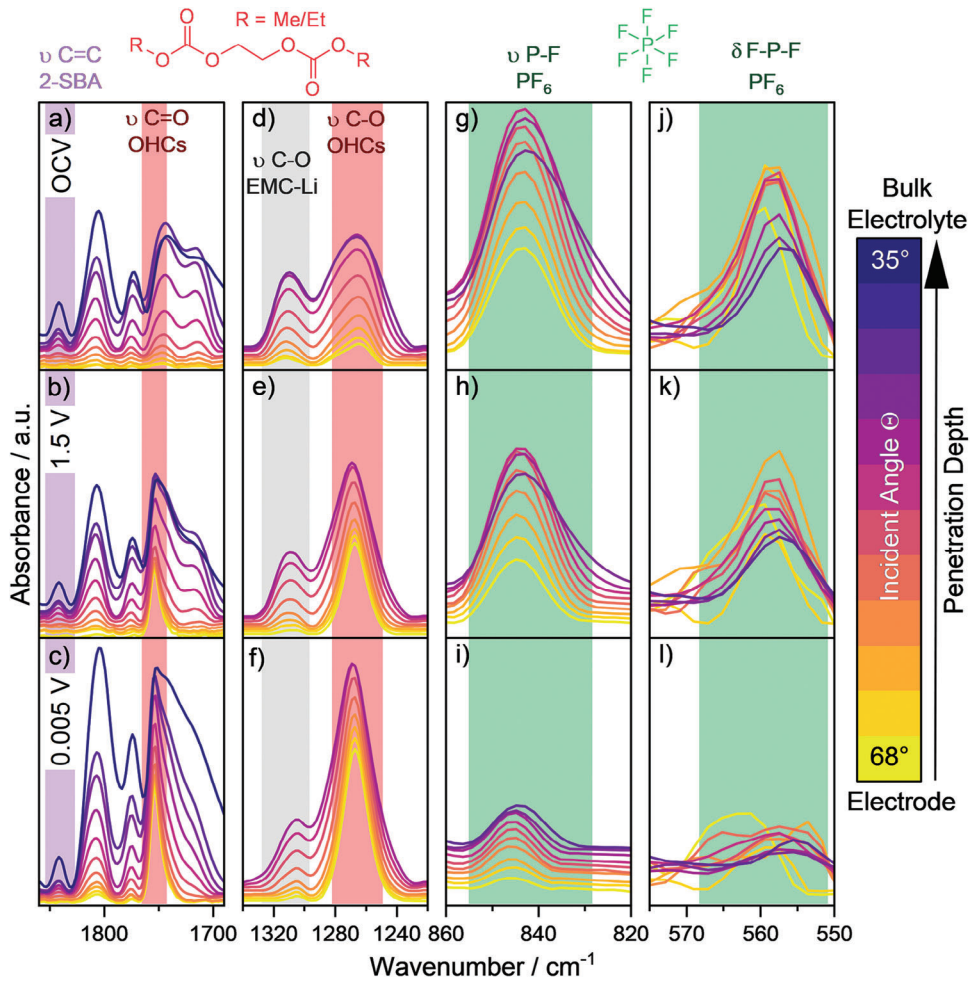

Figure 6. Operando ATR-FTIR spectra of the interphase on a silicon wafer with BE+2-SBA electrolyte during open-circuit-voltage (OCV), at 1.5 V, and after 3 h of 0.005 V constant voltage for a–c) C = O stretch, d–f) C-O stretch, g–i) P-F stretch, and j–l) F-P-F deformation region.

reduction.[17,19] To additionally support this, the vibrational frequencies of different possible degradation products were calculated. The products include the reduced 2-SBA, structures identified by the bulk electrolyte IC-CD-MS analysis, and similar related structures. Detailed calculation results and corresponding molecular structures are shown in Tables S4–S6 (Supporting Information).

The operando ATR-FTIR spectra of the SEI on a Si wafer formed with BE+2-SBA at an incident angles of 68° to 35° are shown in **Figure** 8a–f. In accordance with the results of DFT calculations of infrared frequencies, given in Table Figure S3 (Supporting Information), and ATR-FTIR spectroscopy ex-situ bulk measurements shown in Figure S*12 (Supporting Information), the band at 1844 cm^{-1} in Figure 6a is characteristic for ν(C = O) of the pristine 2-SBA additive. Additionally, the regions 1610 – 1560 cm^{-1} for ν(C = C) (Figure 8a–c) and 810 – 590 cm^{-1} (Figure 8d–f) are characteristic for 2-SBA and the respective degradation products, due to the absence of vibrational bands belonging to BE components. For instance, the band at ≈1590 cm^{-1} corresponds to the E_{2g} ν(C = C) vibration of the aromatic ring of the pristine 2-SBA with a closed anhydride ring.[56] Also, the ν(C-O) vibration corresponding to the (O=)C-O-S(=O)$_2$ group at around 790 cm^{-1} represents the intact 2-SBA with a closed anhydride ring. As can be seen, the intensity and shape of the band are nearly constant at the different cell voltages. Consequently, changing intensities and shapes of other bands are thus mostly related to new components formed on the Si wafer surface.

Generally, these characteristic bands from unique functional groups, such as sulfonates, of the investigated electrolyte additive compared to the rest of the electrolyte components are of high importance to evaluate the spatial structure and composition of the SEI with operando ATR-FTIR spectroscopy. Especially carbonate-based electrolyte components, such as EC or EMC, additives, such as VC or FEC, and their degradation products, such as OHCs, or (organic) lithium carbonates, share very similar vibrational bands, which makes a clear assignment challenging.

DFT vibrational frequency calculations show a red-shift for the E_{2g} band after reduction and anhydride ring-opening, indicating the presence of ring-opened 2-SBA-related structures in the interphase. The anhydride ring-opened structure can be assigned to the band at 1575 cm^{-1} in Figure 8c, which is only visible at low incident angles. The appearance during lithium-ion insertion into the silicon electrode leads to the assumption that the

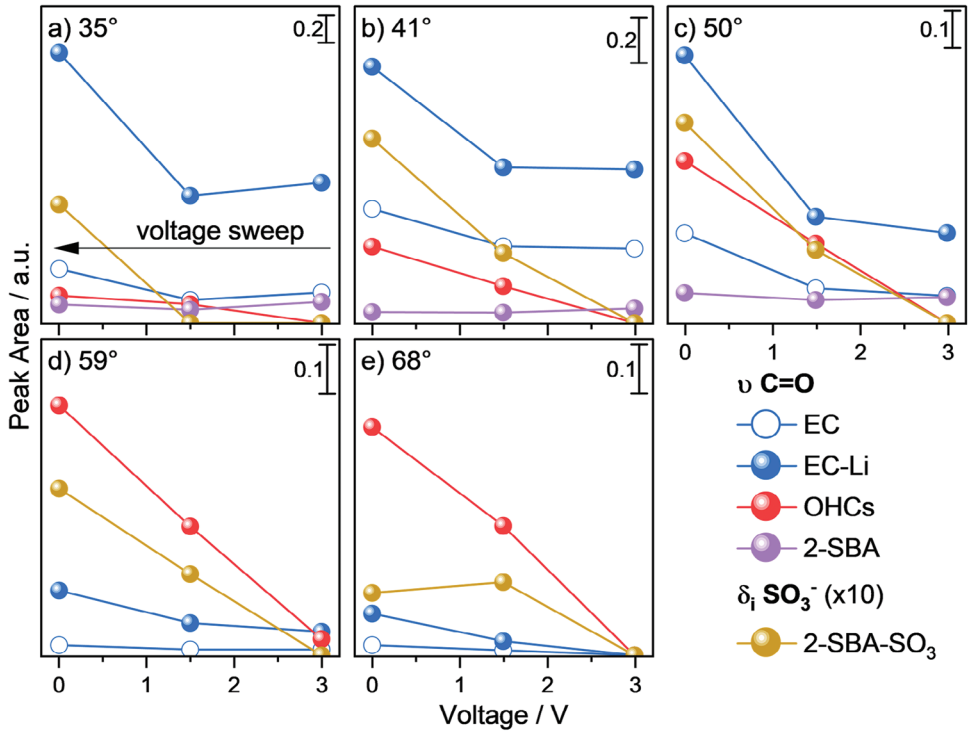

Figure 7. IntegraPeak areas at incident angles of a) 35°, b) 41°, c) 50°, d) 59°, and e) 68° for the vibrational bands of ν(C = O) EC (1774 cm^{-1}), EC coordinated with Li (1806 cm^{-1}), OHCs (1752 cm^{-1}), 2-SBA (1844 cm^{-1}), and $\delta_i(SO_3^-)$ of reduced ring-opened 2-SBA with sulfonate group (82 cm^{-1}). The y-axis offset is normalized to 0 arbitrary units (a.u.), and the band intensity of $\delta_i(SO_3^-)$ is shown with a factor of 10 for increased visibility due to the lower intrinsic intensity compared to ν(C = O).

reduced and ring-opened 2-SBA degradation products are not accumulating directly at the electrode surface but rather on top of the already existing OHCs layer.

Furthermore, the characteristic band for inversion deformation (δ_i) of the SO_3^- group in the 2-SBA degradation products, shown in Figure 8d–f, appear during the constant voltage step at around 620 cm^{-1}. The peak area for the band assigned to $\delta_i(SO_3^-)$ in Figure 7 is strongly increasing during constant voltage at low incident angles, but nearly constant at high incident angles. Thus, it is assumed that the SO_3^- containing 2-SBA degradation products are accumulating on top of the OHC layer.

Further bands, which can be assigned to 2-SBA degradation products are δ(C-H) and δ(C-C) from the aromatic ring, and ν(C-S), which are shifting due to ring-opening of the anhydride. Also, Figure S*13 (Supporting Information) shows that an additional shoulder ≈1330 cm^{-1} appears during constant voltage hold, which can be assigned to CH_2 twisting deformation (δ_{tw}) of an ethoxy group by DFT calculation results, most likely caused by compounds **C** and **D** (see Figure 4) from 2-SBA degradation.

The calculated vibrational frequencies for ν(C=O) of the degradation products with —COOMe or —COOEt moieties are located ≈1740 cm^{-1}, which overlaps with ν(C=O) of EMC and of OHCs, as shown in Figure 7a. Thus, this band may not be suitable for determining the presence or absence of a carboxylate group on the formed 2-SBA degradation products. A schematic of the operando ATR-FTIR results are shown in **Figure 9a** and structures of the 2-SBA degradation products identified with ex-situ IC-CD-MS and operando ATR-FTIR spectroscopy in Figure 9b.

3. Conclusion

The implementation of the SEI-forming electrolyte additive 2-SBA increased the electrochemical performance of high-voltage NMC811||AG+20% SiO_x cells in terms of capacity retention and Coulombic efficiency. This resulted in a significantly improved cell cycle life and accumulated specific energy. By utilizing different operando, ex-situ, and post-mortem analysis techniques as well as DFT calculations, the composition and structure of the interphase formed by 2-SBA and other electrolyte species were elucidated to shed light on the mechanistic working principle of SEI formation. Still, the electrochemical performance of 2-SBA as electrolyte additive in other cell chemistries needs to be evaluated.

Different analytical techniques were complemented to elucidate the reductive degradation mechanism of the 2-SBA additive in the electrolyte and on the silicon oxide surface. Ex-situ IC-CD-MS analysis revealed different degradation products in the bulk electrolyte, which were formed by co-reaction of 2-SBA with EC/EMC transesterification and degradation products. Furthermore, at high-voltage in NMC811||AG+20% SiO_x full cells, an end-stage 2-SBA degradation product was identified, consisting of a benzene ring with a sulfonate and carboxylate group. Those molecules originate from 2-SBA degradation on the anode surface during SEI formation. The elemental SEI composition was characterized with post-mortem EDX analysis, proving the presence of sulfur on the anode surface. Employing the in-house developed operando ATR-FTIR spectroscopy setup, the molecular

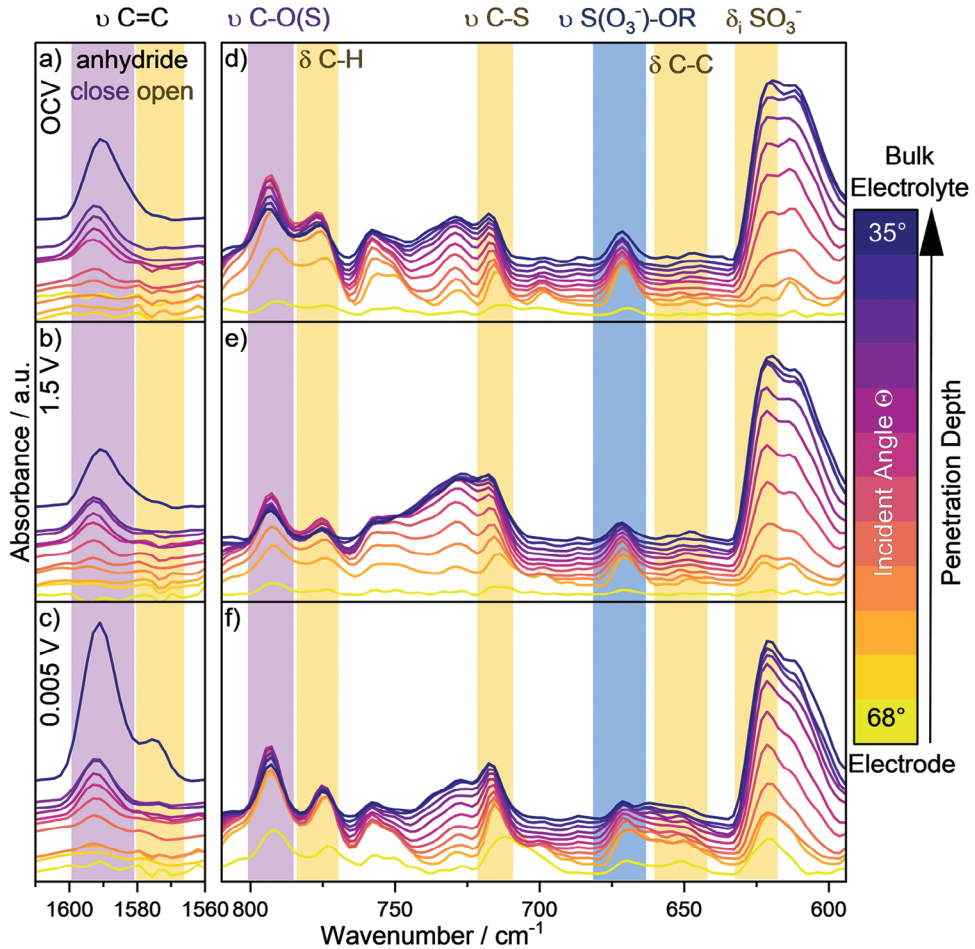

Figure 8. Operando ATR-FTIR spectra of the spectroelectrochemical cell with BE+2-SBA with Si wafer as working and lithium metal as counter electrode in the range of a–c) 1610 – 1560, and d–f) 810 – 610 cm^{-1}.

structure of the SEI formed in the presence of 2-SBA was investigated. These insights into the SEI revealed anhydride ring-opening degradation of 2-SBA after electrochemical reduction. According to the operando ATR-FTIR spectroscopy analysis, different 2-SBA ring-opening products with carboxylate, sulfonate, and sulfinate groups were identified, presented in Figure 9. Analysis of ATR-FTIR spectra at different penetration depths indicates accumulation of the 2-SBA degradation products on top of the OHCs-layer, formed by degradation of other electrolyte component. The results were complemented with DFT calculations, confirming the thermodynamically favored S-O ring-opening mechanism.

4. Experimental Section

Electrolyte Preparation: As baseline electrolyte (BE) 1.00 M $LiPF_6$ (E-Lyte Innovations GmbH, Germany) in EC/EMC (3:7, by weight; E-Lyte Innovations GmbH, Germany) was used. The electrolyte additives, lithium difluorophosphate (LiDFP, TCI Chemicals GmbH, Germany) and 2-Sulfobenzoic anhydride (2-SBA, abcr GmbH, Germany) were added to the electrolyte solution with concentrations of 0.05 M, 0.10 M, or 0.20 M. The electrolytes were prepared and stored in an argon-filled (O_2 and H_2O < 5 ppm) glovebox (MBraun, Germany).

Electrochemical Investigation: For electrochemical investigations multi-layer wounded NMC811||AG+20% SiO_x and NMC811||AG pouch cells, balanced for cell operation ranges up to 4.5 V, were obtained from LiFUN Technology Corporation Limited (Hunan, China) in a sealed and dry state. Before cell assembly, the cells were cut open and dried under reduced pressure at 90 °C overnight. Then the pouch cells were filled with 700 µL electrolyte (corresponding to 4.2 g Ah^{-1} for BE and 200 mAh nominal capacity at 0.1C of the used pouch cells) and afterwards vacuum sealed at 15% of the ambient pressure (GN-HS350V, Gelon Lib Co., Ltd., China) while maintaining a gas pocket in a dry-room (dew point: < −50 °C). After two formation cycles at 0.1C, the cells were cut open, vacuum-sealed directly at the cell stack, and then charge/discharge cycled at 1C (250 mA) until 50% SoH. The cells were charged to a cell voltage cut-off of 4.5 V in a constant-current constant-voltage (CCCV) procedure until the current dropped below 0.01C. Afterward, the cells were then discharged with a CC procedure to a lower cell voltage cut-off of 2.8 V. After the two formation cycles at 0.1C, the cells were cut open, vacuum re-sealed at the cell stack ("degassing"), and reconnected for CCCV charge and CC discharge cycling at 1C. The electrochemical investigations were conducted on a Maccor 4000 battery tester in a 20°C temperature chamber. During operation the cells were clamped with a custom build cell holder, as reported in,[40] to apply a stack pressure of ≈2 bar. For the calculation of the SoH, the fourth overall cycle was used as reference point for maximum capacity. Cyclic voltammetry was performed with 3-electrode Swagelok-type cells with NMC811 or AG+20% SiO_x obtained from the above-mentioned pouch cells as working or counter electrode

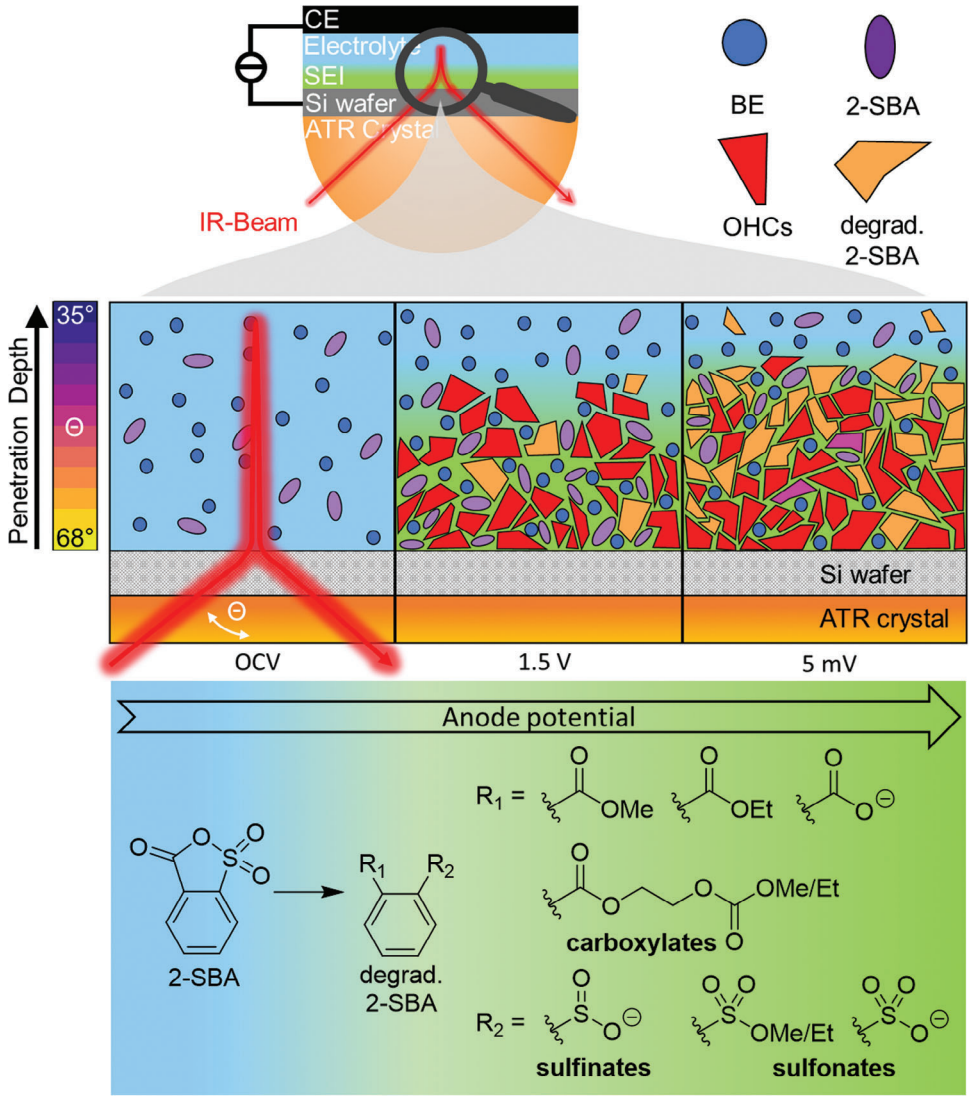

Figure 9. Schematic overview of the proposed SEI composition and corresponding 2-SBA degradation products present in the interphase during SEI formation found by ex-situ IC-CD-MS and operando ATR-FTIR spectroscopy.

and lithium metal reference. Working and counter electrodes were separated by two layers of 13 mm diameter Whatman GF/D separator soaked with 120 µL electrolyte (BE or BE+0.10 M 2-SBA). Additionally, one layer of 10 mm Whatman GF/D was soaked with 30 µL electrolyte (BE or BE+0.10 M 2-SBA). The cells were polarized with a rate of 150 µV s^{-1} to 0.01 V versus $Li|Li^+$ (AG+20% SiO_x as working electrode) and 4.50 V versus $Li|Li^+$ (NMC811 as working electrode) on a potentiostat/galvanostat PGSTAT204 (Metrohm) controlled by NOVA 2.1 software (Metrohm).

Operando ATR FTIR-Spectroscopy: Operando ATR-FTIR measurements were carried out on an Invenio-R with a mercury-cadmium-telluride (MCT) detector on a ZnSe ATR crystal (Bruker, US) and VeeMAX III automatic variable angle specular reflection accessory (PikeTechnologies, US) in an in-house build spectroelectrochemical cell. The cell was designed using the Inventor Professional 2022 (Autodesk, US) and 3D-printed with Composite-X resin (Liqcreate, Netherlands) in a Mars 3 3D-printer (Elegoo, US). The spectral resolution was 4 cm^{-1} and each spectrum was obtained by accumulating 64 sample and 32 background scans. For background scans a second cell without electrolyte was inserted into the spectrometer. All spectra were processed with H_2O correction and extended ATR correction (ATR reflections: 1, ATR angle of incidence: 68° – 35°, mean refractive index of sample: 1.5, material: ZnSe). Additionally, concave rubberband background correction was carried out with 33 iterations to increase comparability at different incident angles. A schematic of the in-house build spectroelectrochemical cell is shown in **Figure 10**. Information and construction files for re-manufacturing the spectroelectrochemical cell setup can be obtained from the authors upon request.

The spectroelectrochemical cell was assembled by pressing a prime CZ-Si(100) double-side polished p-type (Boron-doped) wafer with 1–10 Ω cm resistance and total thickness variation < 10 µm (MicroChemicals, Germany) against the reflective plane of a ZnSe semisphere ATR crystal (25 mm diameter, Bruker, US) with an O-ring and fixed by clamping the cell housing with six screws. Before clamping, Nujol oil (VWR International, US) was added between the Si wafer and ZnSe surface. A round copper foil (30 mm diameter) with a 12 mm diameter hole in the center and with a 5 cm strip to connect cables via crocodile clips was used as current collector. To enhance electrical contact in the center of the wafer, a 13 mm diameter copper mesh was placed in the center-hole of the current collector. Afterward, the glass fiber separator (Whatman GF/D), 300 µL electrolyte, lithium metal as counter electrode, and the current collector with a spring and gaskets were sandwiched and clamped with an external

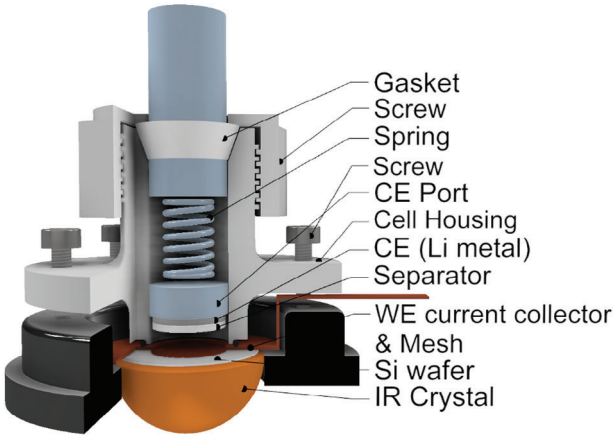

Figure 10. Schematic drawing of the spectroelectrochemical cell.

additional screw. Electrochemical tests were performed with an Autolab PGSTAT204 (Metrohm, Germany) controlled by the NOVA 2.1 software. The cell was polarized from open circuit voltage (OCV) to 0.01 V with a scan rate of 0.15 mV and then held at a constant voltage. The IR measurements were carried out during cell operation. Note that there is a native oxide layer on the silicon wafer surface, resembling the SiO_x particles present in the AG+20% SiO_x anode. Spectra of bulk electrolytes and additives were measured on a Platinum ATR with a diamond crystal (Bruker, US). The IR spectrometer is located in a box with nitrogen atmosphere which is constantly flushed with nitrogen.

Ion Chromatography-Conductivity Detection-Mass Spectrometry (IC-CD-MS): A qualitative analysis of anionic additive-based degradation products was executed on an 850 Professional IC (Metrohm, Switzerland) with conductivity detection (CD) hyphenated to a 6530 Accurate Mass Quadrupole-Time-of-Flight (Q-TOF)-MS (Agilent, US). A Metrosep A Supp 7 column (250 × 4.0 mm, 5 µm; Metrohm) was used for isocratic separation of the anionic compounds at an oven temperature of 65°C and an applied flow rate of 0.7 mL min^{-1} over a total runtime of 30 min. The chromatograms were cut to 5 to 15 min to exclude the conductive salt. All samples were diluted 1:1000 with acetonitrile and the injection volume was set to 65 µL. The eluent consisted of a 3.6/3.4 mM Na_2CO_3/$NaHCO_3$ aqueous solution and acetonitrile in a ratio of 58:42 (v/v). The utilized suppressor was sequentially regenerated by 0.1 M sulfuric acid and rinsed with Milli-Q water. Ionization in the MS was performed in negative electrospray ionization (ESI(-)) mode at a capillary voltage of 3.5 kV. The nebulizer gas was set to 45 psig and drying gas to a flow of 10 L min^{-1} at 350°C. A collision-induced dissociation energy of 30 eV was applied for MS/MS experiments and the mass range was set to *m/z* 70-500 in MS^1 and *m/z* 50-500 in MS^2. Instrument control, data acquisition, and data evaluation were performed for MS with MassHunter Data Acquisition and MassHunter Qualitative Analysis B.08.00 (Agilent, US), while for IC with MagIC Net 3.3 (Metrohm). The developed method is based on Kraft et al. and further parameters and sample preparation were applied according to Henschel et al.[45,57] To protect the MS system from overload by non-ionic substances as well as the conducting salt, the spectra were only acquired between 5 and 15 min. The complete chromatograms, which were acquired by means of CD, are shown in Figure S*9a (Supporting Information) and exemplary MS fragmentation in Figure S*9b (Supporting Information). Possible shifts within the retention times can be explained by the manual start of the MS. Identification of the respective 2-SBA degradation products is based on accurate molecular formula predictions provided by the high-resolution accurate mass (HRAM-)MS system, the fragmentation behavior, and the characteristic sulfur isotope pattern with $^{33}S/^{13}C$ and ^{34}S.

SEM & EDX Analysis: An Auriga electron microscope (Carl Zeiss Microscopy GmbH, Germany) was used for scanning electron microscopy (SEM) imaging. The pictures were obtained with an accelerating voltage of 3 kV and a working distance of 5 mm. Energy-dispersive X-ray (EDX) measurements were carried out at an accelerating voltage of 10 kV using an energy-dispersive X-ray detector (Oxford Instruments, UK). The investigated electrode was taken from a NMC811||AG+20% SiO_x pouch cell charge/discharge cycled with BE+2-SBA (as described above). Prior to SEM and EDX measurements, the electrodes were rinsed with 100 µL dimethyl carbonate (DMC) in an argon-filled glovebox, dried under reduced pressure, and transferred in an air-tight sample chamber.

Theoretical Calculations: Density functional theory (DFT) calculations were carried out using the Gaussian16 package.[58] All geometries were optimized using B3LYP DFT functional and the 6-311++G(3df, 2p) basis set. The effect of a surrounding electrolyte was mimicked by SMD implicit solvation model using parameters for acetone, showing a similar dielectric constant as liquid carbonate-based electrolytes.[15,59–61] The reduction potentials were calculated via the Nernst equation with a lithium-ion coordinated to the additive before and after reduction with the electrical energy and thermal free energy correction. The energies for the putative reactions were calculated and referenced to the additive before reduction. To relate the calculated reduction potential values for the reactions with the $Li|Li^+$ scale and graphite potential (0.1 V vs $Li|Li^+$), a constant shift of -1.4 V was applied.[15,59,62–63] After geometry optimization, the calculated IR frequencies were used to support the ATR-FTIR spectra interpretations.

Supporting Information

Supporting Information is available from the Wiley Online Library or from the author.

Acknowledgements

Financial support from the German Federal Ministry for Education and Research within the project "EFoBatt" (grant number 13XP5129) is gratefully acknowledged.

Open access funding enabled and organized by Projekt DEAL.

Conflict of Interest

The authors declare no conflict of interest.

Data Availability Statement

The data that support the findings of this study are available from the corresponding author upon reasonable request.

Keywords

2-sulfobenzoic acid anhydride, lithium-ion batteries, operando ATR-FTIR spectroscopy, silicon oxide, solid-electrolyte interphase

Received: October 20, 2023
Revised: November 21, 2023
Published online: December 6, 2023

[1] P. Meister, H. Jia, J. Li, R. Kloepsch, M. Winter, T. Placke, *Chem. Mater.* **2016**, *28*, 7203.
[2] A. Gomez-Martin, M. M. Gnutzmann, E. Adhitama, L. Frankenstein, B. Heidrich, M. Winter, T. Placke, *Adv. Sci.* **2022**, *9*, 2201742.
[3] F. Holtstiege, A. Wilken, M. Winter, T. Placke, *Phys. Chem. Chem. Phys.* **2017**, *19*, 25905.

[4] G. M. Overhoff, R. Nölle, V. Siozios, M. Winter, T. Placke, *Batteries Supercaps* **2021**, *4*, 1163.
[5] X. Zuo, J. Zhu, P. Müller-Buschbaum, Y.-J. Cheng, *Nano Energy* **2017**, *31*, 113.
[6] J. Asenbauer, T. Eisenmann, M. Kuenzel, A. Kazzazi, Z. Chen, D. Bresser, *Sustainable Energy Fuels* **2020**, *4*, 5387.
[7] M. A. Al-Maghrabi, J. Suzuki, R. J. Sanderson, V. L. Chevrier, R. A. Dunlap, J. R. Dahn, *J. Electrochem. Soc.* **2013**, *160*, A1587.
[8] K. Kitada, O. Pecher, P. C. M. M. Magusin, M. F. Groh, R. S. Weatherup, C. P. Grey, *J. Am. Chem. Soc.* **2019**, *141*, 7014.
[9] M. Weiling, F. Pfeiffer, M. Baghernejad, *Adv. Energy Mater.* **2022**, *12*, 2202504.
[10] A. M. Tripathi, W.-N. Su, B. J. Hwang, *Chemical Society Reviews* **2018**, *47*, 736.
[11] M. Winter, *The Solid Electrolyte Interphase – The Most Important and the Least Understood Solid Electrolyte in Rechargeable Li Batteries* **2009**, *223*, 1395.
[12] J. Maibach, J. Rizell, A. Matic, N. Mozhzhukhina, *ACS Materials Letters* **2023**, *5*, 2431.
[13] F. Pfeiffer, D. Diddens, M. Weiling, M. Baghernejad, *ACS Appl. Mater. Interfaces* **2023**, *15*, 6676.
[14] P. P. R. M. L. Harks, F. M. Mulder, P. H. L. Notten, *J. Power Sources* **2015**, *288*, 92.
[15] F. Pfeiffer, D. Diddens, M. Weiling, L. Frankenstein, S. Kühn, I. Cekic-Laskovic, M. Baghernejad, *Adv. Energy Mater.* **2023**, *13*, 2300827.
[16] F. Shi, P. N. Ross, G. A. Somorjai, K. Komvopoulos, *J. Phys. Chem. C* **2017**, *121*, 14476.
[17] P. Jankowski, N. Lindahl, J. Weidow, W. Wieczorek, P. Johansson, *ACS Appl. Energy Mater.* **2018**, *1*, 2582.
[18] B. Tong, Z. Song, H. Wan, W. Feng, M. Armand, J. Liu, H. Zhang, Z. Zhou, *InfoMat* **2021**, *3*, 1364.
[19] P. Jankowski, M. Poterala, N. Lindahl, W. Wieczorek, P. Johansson, *J. Mater. Chem. A* **2018**, *6*, 22609.
[20] C. Wölke, B. A. Sadeghi, G. G. Eshetu, E. Figgemeier, M. Winter, I. Cekic-Laskovic, *Adv. Mater. Interfaces* **2022**, *9*, 2101898.
[21] M. Kubot, L. Frankenstein, E. Muschiol, S. Klein, M. Esselen, M. Winter, S. Nowak, J. Kasnatscheew, *ChemSusChem* **2023**, *16*, 202202189.
[22] S. Klein, P. Harte, S. Van Wickeren, K. Borzutzki, S. Röser, P. Bärmann, S. Nowak, M. Winter, T. Placke, J. Kasnatscheew, *Cell Rep. Phys. Sci* **2021**, *2*, 100521.
[23] C. Wang, L. Yu, W. Fan, J. Liu, L. Ouyang, L. Yang, M. Zhu, *ACS Appl. Energy Mater.* **2018**, *1*, 2647.
[24] S. Klein, P. Bärmann, T. Beuse, K. Borzutzki, J. E. Frerichs, J. Kasnatscheew, M. Winter, T. Placke, *ChemSusChem* **2021**, *14*, 595.
[25] I. Buchberger, S. Seidlmayer, A. Pokharel, M. Piana, J. Hattendorff, P. Kudejova, R. Gilles, H. A. Gasteiger, *J. Electrochem. Soc.* **2015**, *162*, A2737.
[26] M. F. Börner, M. H. Frieges, B. Späth, K. Spütz, H. H. Heimes, D. U. Sauer, W. Li, *Cell Rep. Phys. Sci.* **2022**, *3*, 101095.
[27] W. Li, H. Zhang, B. Van Vlijmen, P. Dechent, D. U. Sauer, *Energy Storage Mater.* **2022**, *53*, 453.
[28] L. Haneke, J. E. Frerichs, A. Heckmann, M. M. Lerner, T. Akbay, T. Ishihara, M. R. Hansen, M. Winter, T. Placke, *J. Electrochem. Soc.* **2020**, *167*, 140526.
[29] J. E. Harlow, S. L. Glazier, J. Li, J. R. Dahn, *J. Electrochem. Soc.* **2018**, *165*, A3595.
[30] J. C. Burns, X. Xia, J. R. Dahn, *J. Electrochem. Soc.* **2013**, *160*, A383.
[31] B. Heidrich, L. Pritzlaff, M. Börner, M. Winter, P. Niehoff, *J. Electrochem. Soc.* **2022**, *169*, 030533.
[32] S. L. Dreyer, K. R. Kretschmer, D. Tripkovic, A. Mazilkin, R. Chukwu, R. Azmi, P. Hartmann, M. Bianchini, T. Brezesinski, J. Janek, *Adv. Mater. Interfaces* **2022**, *9*, 2101100.
[33] S. Neudeck, F. Strauss, G. Garcia, H. Wolf, J. Janek, P. Hartmann, T. Brezesinski, *Chem. Commun.* **2019**, *55*, 2174.
[34] B. Liu, H. Zhou, C. Yin, H. Guan, J. Li, *Electrochim. Acta* **2019**, *321*, 134690.
[35] X. Wu, L. Ma, J. Liu, K. Zhao, D. L. Wood, Z. Du, *J. Power Sources* **2022**, *545*, 231863.
[36] T. Boetticher, A. Adamson, S. Buechele, E. D. Alter, M. Metzger, *J. Electrochem. Soc.* **2023**, *170*, 060507.
[37] S. Buechele, E. Logan, T. Boulanger, S. Azam, A. Eldesoky, W. Song, M. B. Johnson, M. Metzger, *J. Electrochem. Soc.* **2023**, *170*, 010518.
[38] T. Boulanger, A. Eldesoky, S. Buechele, T. Taskovic, S. Azam, C. Aiken, E. Logan, M. Metzger, *J. Electrochem. Soc.* **2022**, *169*, 040518.
[39] H. Li, N. Zhang, J. Li, J. R. Dahn, *J. Electrochem. Soc.* **2018**, *165*, A2985.
[40] J.-P. Schmiegel, M. Leißing, F. Weddeling, F. Horsthemke, J. Reiter, Q. Fan, S. Nowak, M. Winter, T. Placke, *J. Electrochem. Soc.* **2020**, *167*, 060516.
[41] J. Xia, R. Petibon, D. Xiong, L. Ma, J. R. Dahn, *J. Power Sources* **2016**, *328*, 124.
[42] K. P. C. Yao, J. S. Okasinski, K. Kalaga, J. D. Almer, D. P. Abraham, *Adv. Energy Mater.* **2019**, *9*, 1803380.
[43] R. Petibon, E. C. Henry, J. C. Burns, N. N. Sinha, J. R. Dahn, *J. Electrochem. Soc.* **2014**, *161*, A66.
[44] K. Kim, I. Park, S.-Y. Ha, Y. Kim, M.-H. Woo, M.-H. Jeong, W. C. Shin, M. Ue, S. Y. Hong, N.-S. Choi, *Electrochim. Acta* **2017**, *225*, 358.
[45] J. Henschel, F. Horsthemke, Y. P. Stenzel, M. Evertz, S. Girod, C. Lürenbaum, K. Kösters, S. Wiemers-Meyer, M. Winter, S. Nowak, *J. Power Sources* **2020**, *447*, 227370.
[46] J. Henschel, C. Peschel, S. Klein, F. Horsthemke, M. Winter, S. Nowak, *Angew. Chem., Int. Ed.* **2020**, *59*, 6128.
[47] G. Gachot, S. Grugeon, M. Armand, S. Pilard, P. Guenot, J.-M. Tarascon, S. Laruelle, *J. Power Sources* **2008**, *178*, 409.
[48] R. Jung, M. Metzger, F. Maglia, C. Stinner, H. A. Gasteiger, *J. Electrochem. Soc.* **2017**, *164*, A1361.
[49] K. Guo, S. Qi, H. Wang, J. Huang, M. Wu, Y. Yang, X. Li, Y. Ren, J. Ma, *Small Sci.* **2022**, *2*, 2100107.
[50] M. Kubot, B. Von Holtum, M. Winter, S. Wiemers-Meyer, S. Nowak, *J. Electrochem. Soc.* **2022**, *169*, 110534.
[51] C.-C. Su, M. He, C. Peebles, L. Zeng, A. Tornheim, C. Liao, L. Zhang, J. Wang, Y. Wang, Z. Zhang, *ACS Appl. Mater. Interfaces* **2017**, *9*, 30686.
[52] I. A. Shkrob, D. P. Abraham, *J. Phys. Chem. C* **2016**, *120*, 15119.
[53] H. Zhao, J. Wang, H. Shao, K. Xu, Y. Deng, *Energy Environ. Mater.* **2022**, *5*, 327.
[54] F. Shi, P. N. Ross, H. Zhao, G. Liu, G. A. Somorjai, K. Komvopoulos, *J. Am. Chem. Soc.* **2015**, *137*, 3181.
[55] T. Sasaki, T. Abe, Y. Iriyama, M. Inaba, Z. Ogumi, *J. Power Sources* **2005**, *150*, 208.
[56] M. Preuss, F. Bechstedt, *Phys. Rev. B* **2006**, *73*, 155413.
[57] V. Kraft, M. Grützke, W. Weber, M. Winter, S. Nowak, *J. Chromatogr. A* **2014**, *1354*, 92.
[58] M. J. Frisch, G. W. Trucks, H. B. Schlegel, G. E. Scuseria, M. A. Robb, J. R. Cheeseman, G. Scalmani, V. Barone, G. A. Petersson, H. Nakatsuji, X. Li, M. Caricato, A. V. Marenich, J. Bloino, B. G. Janesko, R. Gomperts, B. Mennucci, H. P. Hratchian, J. V. Ortiz, A. F. Izmaylov, J. L. Sonnenberg, Williams, F. Ding, F. Lipparini, F. Egidi, J. Goings, B. Peng, A. Petrone, T. Henderson, D. Ranasinghe, et al., Gaussian 16 Rev. C.01, Wallingford, CT **2016**.
[59] O. Borodin, M. Olguin, C. E. Spear, K. W. Leiter, J. Knap, *Nanotechnology* **2015**, *26*, 354003.
[60] D. S. Hall, J. Self, J. R. Dahn, *J. Phys. Chem. C* **2015**, *119*, 22322.
[61] A. V. Marenich, C. J. Cramer, D. G. Truhlar, *J. Phys. Chem. B* **2009**, *113*, 6378.
[62] O. Borodin, X. Ren, J. Vatamanu, A. Von Wald Cresce, J. Knap, K. Xu, *Acc. Chem. Res.* **2017**, *50*, 2886.
[63] P. Jankowski, W. Wieczorek, P. Johansson, *J. Mol. Model.* **2016**, *23*, 6.